Phase behavior of an amphiphilic fluid

Martin Schoen,[1,2,*] Stefano Giura,[1] and Sabine H. L. Klapp[3]

[1]*Stranski-Laboratorium für Physikalische und Theoretische Chemie, Fakultät für Mathematik und Naturwissenschaften, Technische Universität Berlin, Straße des 17. Juni 115, 10623 Berlin, Germany*

[2]*Department of Chemical and Biomolecular Engineering, Engineering Building I, Box 7905, North Carolina State University, 911 Partners Way, Raleigh, North Carolina 27695, USA*

[3]*Institut für Theoretische Physik, Fakultät für Mathematik und Naturwissenschaften, Technische Universität Berlin, Hardenbergstr. 36, 10623 Berlin, Germany*

(Received 15 August 2013; revised manuscript received 27 November 2013; published 31 January 2014)

We invoke mean-field density functional theory (DFT) to investigate the phase behavior of an amphiphilic fluid composed of a hard-sphere core plus a superimposed anisometric Lennard-Jones perturbation. The orientation dependence of the interactions consists of a contribution analogous to the interaction potential between a pair of "spins" in the classical, three-dimensional Heisenberg fluid and another one reminiscent of the interaction between (electric or magnetic) point dipoles. At fixed orientation both contributions are short-range in nature decaying as r^{-6} (r being the separation between the centers of mass of a pair of amphiphiles). Based upon two mean-field-like approximations for the pair correlation function that differ in the degree of sophistication we derive expressions for the phase boundaries between various isotropic and polar phases that we solve numerically by the Newton-Raphson method. For sufficiently strong coupling between the Heisenberg "spins" both mean-field approximations generate three topologically different and generic types of phase diagrams that are observed in agreement with earlier work [see, for example, Tavares *et al.*, Phys. Rev. E **52**, 1915 (1995)]. Whereas the dipolar contribution alone is incapable of stabilizing polar phases on account of its short-range nature it is nevertheless important for details of the phase diagram such as location of the gas-isotropic liquid critical point, triple, and tricritical points. By tuning the dipolar coupling constant suitably one may, in fact, switch between topologically different phase diagrams. Employing also Monte Carlo simulations in the isothermal-isobaric ensemble the general topology of the DFT phase diagrams is confirmed.

DOI: 10.1103/PhysRevE.89.012310 PACS number(s): 61.25.Em, 64.60.A−, 64.60.fd, 05.10.Ln

I. INTRODUCTION

Amphiphiles are chemical compounds consisting of moieties with antithetic properties. An example are surfactants that are composed of hydrophilic and hydrophobic parts. Because of the presence of moieties with conflictive properties in the same molecule amphiphiles exhibit a rather rich phase behavior and a large variety of different structures that can form through self-assembly [1]. A special class of amphiphiles are Janus particles which are particles with chemically distinct surfaces. These surfaces cause an orientation dependence of the interaction potential [2,3]. Advances in chemical synthesis nowadays permit to fabricate Janus particles with sizes all the way down to the nanometer length scale [4].

In a recent study we investigated the formation of ordered liquid phases in an amphiphilic fluid [5]. Polarity of the ordered phase is promoted by orientation dependent intermolecular interactions resembling those characteristic of the interaction between a pair of "spins" in the classical, three-dimensional Heisenberg model (coupling constant ε_{H}) with superimposed "dipolar" interactions (coupling constant ε_{D}). In our model both the "spin-spin" and the "dipole-dipole" interactions are short-range, that is at fixed relative orientation of an amphiphilic pair the intermolecular interaction potential decays proportional to r^{-6} where r denotes the distance between the centers of mass of the amphiphiles. As was argued earlier by Erdmann *et al.*, who introduced this model, chains of amphiphiles should form under favorable thermodynamic conditions if both ε_{H} and ε_{D} are positive [6]. Ideally, in these chains the North Pole of any given amphiphile would then be facing the South Pole of its neareat neighbor along the chain and vice versa (see Fig. 1 and Table 1 of Ref. [6]). Employing Landau theory we could show that in our model a line of critical points exists separating isotropic from polar liquid phases similar to the Curie line in ferroelectrics [5]. However, so far it is not known whether and how these second-order phase transitions interfere with other fluid-fluid transitions such as condensation.

In our earlier study we could also demonstrate that the formation of the ordered phase is almost exclusively driven by the Heisenberg contribution to the interaction potential whereas the "dipolar" one is negligible [see Eqs. (3.26) and (3.33) of Ref. [5]]. This is consistent with the observation that our model pertains to the three-dimensional Heisenberg universality class [7]. The negligible influence of the "dipolar" part of the interaction potential on the formation of a polar liquid phase is also not surprising because of the short-range character of the "dipolar" interactions. This is in contrast to fluids in which molecules carry true electric or magnetic (point) dipoles where at fixed relative orientation the interaction potential is long range decaying in proportion to r^{-3} instead [8–10].

The long-range nature of the interaction potential between electric or magnetic dipoles has fascinated many researchers in the past because it poses special problems to theoretical approaches. For example, Groh and Dietrich demonstrated that in the polar phase the free-energy density depends crucially

*martin.schoen@tu-berlin.de

on the shape of the domain under consideration and also on the dielectric permittivity of the surrounding medium into which these domains are embedded [11]. By means of integral-equation approaches and a related density functional theory (DFT) Klapp and coworkers [12,13] could demonstrate later that for a system of dipolar hard spheres the ferroelectric fluid phase could be suppressed in favor of a stable ferroelectric solid [14,15]. In a later study Range and Klapp [16] employed modified mean-field (MMF) DFT [11,17–19] to investigate the full phase behavior of binary hard-sphere mixtures with embedded point dipoles. In addition, dipolar fluids under nanoconfinement conditions have also been investigated by means of integral-equation approaches [20], DFT [21], and Monte Carlo (MC) computer simulations [22].

The variety of fascinating scientific problems tackled in these earlier works on dipolar fluids clearly exemplifies the richness of the physics of these fluids. Similarly, quite a bit of attention has been devoted to fluids in which the orientation dependence of the intermolecular interactions is purely of the Heisenberg type [19,23–33]. In view of the present study the earlier works by Tavares *et al.* [19] and of Weis *et al.* [31] are particularly relevant because they show that for a ferromagnetic Heisenberg fluid the Curie line separating isotropic and polar liquid phases may either end in a tricritical or in a critical end point where the specific situation encountered depends on the coupling strength of the "spin-spin" interaction. On the other hand, Lomba *et al.* ruled out the termination of the Curie line at a tricritical point [30]. Using a combination of computer simulations and integral equations these latter authors suggest that the Curie line terminates at a critical end point instead.

In all these earlier works that we briefly reviewed here the orientation dependence of the intermolecular interactions is exclusively either dipolar in nature or of the Heisenberg type. On the contrary, in our model both orientation dependencies of the intermolecular interactions are present simultaneously. In fact, as we shall demonstrate and discuss here both contributions cooperate in a nontrivial fashion. As a consequence the phase behavior of the amphiphilic fluid is characterized by subtle effects. Even though the (short-range) "dipolar" contribution to the overall interaction potential does not seem to affect the isotropic-polar transition in the liquid phase to any significant extent, the natural question arises: Is that also true for the *entire* phase diagram of the amphiphilic fluid? Another motivation for carrying out the present work is to investigate in more detail the role of the specific mean-field approximation needed to evaluate the expression for the excess free energy in the DFT approach on which our study is based. For example, we already showed that at MMF level the "dipolar" coupling constant enters the description of the Curie line quadratically in leading order whereas this is not so for a simplified version of the mean-field DFT. What impact does this simplified version of the theory then have on other parts of the phase diagram of the amphiphilic fluid?

To address these questions we have organized the remainder of our paper as follows. We begin in Sec. II by introducing the model on which this study is based. Section III is devoted to a summary of the DFT approaches employed here. Some mathematical details of key equations and details of the numerical procedure to solve them are deferred to Appendix A and B, respectively. A detailed account of our results is given in Sec. IV. In Sec. V we compare our DFT results with MC simulations carried out in the isothermal-isobaric ensemble. Finally, we discuss our results and put them into perspective in the concluding Sec. VI.

II. MODEL

We consider a fluid composed of N amphiphiles interacting with each other in a pairwise additive fashion. On account of the amphiphilic nature of the molecules their interaction potential depends on their orientations ω_1 and ω_2 and the distance vector $\boldsymbol{r}_{12}$ connecting the centers of a molecular pair. Here and below $\omega_i = (\theta_i, \phi_i)$ $(i = 1,2)$ where θ_i and ϕ_i are Euler angles specifying the orientation of the prolate amphiphile i. More specifically, we assume the intermolecular interaction to be described by the potential

$$\varphi_{\text{tot}}(\boldsymbol{r}_{12},\omega_1,\omega_2) = \varphi_{\text{hs}}(r_{12}) + \varphi(\boldsymbol{r}_{12},\omega_1,\omega_2) \tag{2.1}$$

where $r_{12} = |\boldsymbol{r}_{12}|$ and

$$\varphi_{\text{hs}}(r_{12}) = \begin{cases} \infty, & r_{12} < \sigma \\ 0, & r_{12} \geqslant \sigma \end{cases} \tag{2.2}$$

is the interaction potential between hard spheres of diameter σ. Moreover,

$$\varphi(\boldsymbol{r}_{12},\omega_1,\omega_2) = \varphi_{\text{iso}}(r_{12}) + \varphi_{\text{anis}}(\boldsymbol{r}_{12},\omega_1,\omega_2) \tag{2.3}$$

may be thought of as a perturbation due to longer-range (compared with the vanishing range of φ_{hs}) orientation dependent interactions. These longer-range anisotropic interactions between an amphiphilic pair consist of an isotropic part which we model via the standard Lennard-Jones potential

$$\begin{aligned} \varphi_{\text{iso}}(r_{12}) &= 4\varepsilon\left[\left(\frac{\sigma}{r_{12}}\right)^{12} - \left(\frac{\sigma}{r_{12}}\right)^{6}\right] \\ &\equiv \varphi_{\text{rep}}(r_{12}) + \varphi_{\text{att}}(r_{12}) \end{aligned} \tag{2.4}$$

In Eq. (2.4), φ_{rep} and φ_{att} represent repulsive and attractive contributions and ε is the depth of the attractive well of φ_{iso}.

The anisotropic part of the perturbation potential given in Eq. (2.3) is described by

$$\varphi_{\text{anis}}(\boldsymbol{r}_{12},\omega_1,\omega_2) = \varphi_{\text{att}}(r_{12})\,\Psi(\widehat{\boldsymbol{r}}_{12},\omega_1,\omega_2) \tag{2.5}$$

and therefore has the same distance dependence as the attractive part of φ_{iso} such that φ_{anis} is short range. In Eq. (2.5) and below the caret is used to indicate a unit vector. The orientation dependence of the interaction between an amphiphilic pair enters Eq. (2.3) via the anisotropy function [see Eq. (2.5)]

$$\Psi(\widehat{\boldsymbol{r}}_{12},\omega_1,\omega_2) = -(4\pi)^{3/2}\left(\sqrt{3}\,\varepsilon_{\text{H}}\,\Phi_{110} + \varepsilon_{\text{D}}\,\Phi_{112}\right) \tag{2.6}$$

where ε_{H} and ε_{D} are coupling constants and

$$\begin{aligned} \Phi_{l_1 l_2 l}(\omega_1,\omega_2,\omega) \equiv \sum_{m_1 m_2 m} & C(l_1 l_2 l; m_1 m_2 m) \\ & \times Y_{l_1 m_1}(\omega_1)\, Y_{l_2 m_2}(\omega_2)\, Y^*_{lm}(\omega) \end{aligned} \tag{2.7}$$

is a rotational invariant [34,35].

In the previous expression $C(l_1 l_2 l; m_1 m_2 m)$ is a Clebsch-Gordan coefficient, Y is a spherical harmonic, and ω denotes

the set of Euler angles needed to specify the orientation of $\widehat{\boldsymbol{r}}_{12}$ in a space-fixed frame of reference. The asterisk on the last term in Eq. (2.7) denotes the complex conjugate. Integers l_i $(i = 1,2)$ and l on the one hand and m_i and m on the other hand are related because $m_i \in [-l_i, \ldots, l_i]$ and $m \in [-l, \ldots, l]$. According to Eqs. (A.130) and (A.131) of Ref. [35] the Clebsch-Gordan coefficients vanish unless $m = m_1 + m_2$ and the triangle relation $|l_1 - l_2| \leqslant l \leqslant l_1 + l_2$ are satisfied simultaneously. Using these properties and Eq. (2.7) it turns out that the two rotational invariants on the right side of Eq. (2.6) may be recast as [see also Eq. (A.62) of Ref. [35]]:

$$\Phi_{110} = -(4\pi)^{-3/2}\sqrt{3}\widehat{\boldsymbol{u}}(\omega_1)\cdot\widehat{\boldsymbol{u}}(\omega_2), \tag{2.8a}$$

$$\Phi_{112} = -(4\pi)^{-3/2}\sqrt{\frac{15}{2}}\{3[\widehat{\boldsymbol{u}}(\omega_1)\cdot\widehat{\boldsymbol{r}}_{12}][\widehat{\boldsymbol{u}}(\omega_2)\cdot\widehat{\boldsymbol{r}}_{12}] - \widehat{\boldsymbol{u}}(\omega_1)\cdot\widehat{\boldsymbol{u}}(\omega_2)\}, \tag{2.8b}$$

where $\widehat{\boldsymbol{u}}$ is a unit vector describing the orientation of an amphiphile. In Eqs. (2.8) we have dropped the arguments of the rotational invariants for notational convenience.

From Eqs. (2.8) and for positive values of the coupling constants ε_{H} and ε_{D} it is then apparent that the anisotropic part of our perturbation potential [see Eq. (2.5)] consists of a contribution corresponding to the interaction between "spins" in a classical, three-dimensional Heisenberg fluid in the absence of a magnetic field [see Eq. (2.8a)] and a second contribution reminiscent of the potential between a pair of electrostatic point dipoles [see Eq. (2.8b)]. To realize the latter we remind the reader that $\varphi_{\mathrm{att}} < 0$ in Eq. (2.5). However, it needs to be emphasized at this stage that at fixed orientation the distance dependence of the anisotropic interaction between an amphiphilic pair is short-range in the model that we adopt in this work. This can easily be seen from Eqs. (2.4) and (2.5), which reveal that for fixed ω_1, ω_2, and ω, $\varphi_{\mathrm{anis}} \propto r_{12}^{-6}$. This short-range character of φ_{anis} is particularly convenient in the development of the mean-field DFT on which this work is based. Moreover, we notice that the amphiphiles are not exactly spherical but are, in fact, ellipsoids of revolution on account of the anisotropy function which shifts the zero of φ depending on the relative orientation of an amphiphilc pair. However, the aspect ratio of the ellipsoids is usually small and amounts typically to 1.20–1.30 depending on the values of ε_{H} and ε_{D}.

III. DENSITY FUNCTIONAL THEORY

For a given temperature T, chemical potential μ, and in the absence of external fields thermodynamic equilibrium states of the model introduced in Sec. II are given by minima of the grand potential functional [see, for example, Eq. (1) of Ref. [19]]

$$\Omega[\rho(\boldsymbol{r},\omega)] = \mathcal{F}[\rho(\boldsymbol{r},\omega)] - \mu\int d\boldsymbol{r}\, d\omega\, \rho(\boldsymbol{r},\omega), \tag{3.1}$$

where $\mathcal{F}$ is the total free energy functional and $\rho(\boldsymbol{r},\omega)$ is the orientation dependent local density. For the interaction potential φ_{tot} introduced in Eqs (2.1)–(2.6) we can decompose $\mathcal{F}$ into three contributions according to

$$\mathcal{F} = \mathcal{F}^{\mathrm{hs}} + \Delta\mathcal{F}^{\mathrm{or}} + \Delta\mathcal{F}^{\mathrm{ex}}, \tag{3.2}$$

where $\Delta\mathcal{F}^{\mathrm{or}}$ is the difference in free energy due to a deviation of the orientational distribution $\alpha(\omega)$ in a polar fluid from that of an isotropic one, $\mathcal{F}^{\mathrm{hs}}$ is free energy of the hard-sphere reference fluid, and $\Delta\mathcal{F}^{\mathrm{ex}}$ represents the change in free energy (relative to $\mathcal{F}^{\mathrm{hs}}$) caused by the perturbation φ [see Eq. (2.3)].

A. Free-energy contributions

In this work we employ two types of mean-field approximations for the excess part of the free-energy functional $\Delta\mathcal{F}^{\mathrm{ex}}$. Within the simple mean-field (SMF) treatment, $\Delta\mathcal{F}^{\mathrm{ex}}$ is linear in the perturbation φ. Specifically, one has [5]

$$\beta\Delta\mathcal{F}_{\mathrm{s}}^{\mathrm{ex}} = \frac{\beta}{2}\int_{r_{12}\geqslant\sigma} d\boldsymbol{r}_1\, d\boldsymbol{r}_2 \int d\omega_1\, d\omega_2\, \rho(\boldsymbol{r}_1,\omega_1)\,\rho(\boldsymbol{r}_2,\omega_2) \times \varphi(\boldsymbol{r}_{12},\omega_1,\omega_2), \tag{3.3}$$

where $\beta \equiv 1/k_{\mathrm{B}}T$ with k_{B} being Boltzmann's constant. In the somewhat more sophisticated modified mean-field (MMF) approach, the perturbation potential enters through the Mayer f function, that is essentially through the Boltzmann factor for an amphiphilic pair. Explicitly, one has

$$\beta\Delta\mathcal{F}_{\mathrm{m}}^{\mathrm{ex}} = \frac{1}{2}\int_{r_{12}\geqslant\sigma} d\boldsymbol{r}_1\, d\boldsymbol{r}_2 \int d\omega_1\, d\omega_2\, \rho(\boldsymbol{r}_1,\omega_1)\,\rho(\boldsymbol{r}_2,\omega_2) \times f(\boldsymbol{r}_{12},\omega_1,\omega_2), \tag{3.4}$$

where

$$\begin{aligned} f(\boldsymbol{r}_{12},\omega_1,\omega_2) &\equiv \exp[-\beta\varphi(\boldsymbol{r}_{12},\omega_1,\omega_2)] - 1 \\ &= \exp[-\beta\varphi_{\mathrm{iso}}(r_{12})] \\ &\quad\times \exp[-\beta\varphi_{\mathrm{anis}}(\boldsymbol{r}_{12},\omega_1,\omega_2)] - 1 \end{aligned} \tag{3.5}$$

is the orientation-dependent Mayer f function [35] which we have factorized into a spherically symmetric part proportional to φ_{iso} and an orientation-dependent contribution proportional to φ_{anis}.

Next, we realize that for a homogeneous bulk phase the orientation dependent local densities appearing in the integrand of Eqs. (3.3) and (3.4) can be recast as

$$\rho(\boldsymbol{r}_k,\omega_k) = \rho\alpha(\omega_k), \quad k = 1,2, \tag{3.6}$$

where ρ is the (mean) number density and the orientation distribution function $\alpha(\omega_k)$ must satisfy the normalization condition

$$\int d\omega_k\, \alpha(\omega_k) = 1, \quad k = 1,2. \tag{3.7}$$

In isotropic phases $\alpha(\omega_k)$ is constant such that Eq. (3.7) implies $\alpha(\omega_k) = 1/4\pi$ thereby reflecting full rotational symmetry. Because the amphiphiles have uniaxial symmetry [see Eqs. (2.5)–(2.8)] polar phases forming in our model system will have this symmetry as well. Here we notice that there is cylindrical symmetry of $\alpha(\omega)$ with respect to the so-called director which represents the net orientation of all the spins of the amphiphiles. As in our previous work [5]

we therefore expand $\alpha(\omega)$ in terms of Legendre polynomials $\{P_l(\cos\theta)\}$ according to

$$2\pi\alpha(\omega) \equiv \overline{\alpha}(\cos\theta) = \frac{1}{2} + \sum_{l=1}^{\infty} \alpha_l P_l(\cos\theta), \tag{3.8}$$

where the set of expansion coefficients $\{\alpha_l\}$ is related to the set of order parameters $\{\mathcal{P}_l\}$ via the expression

$$\alpha_l = \frac{2l+1}{2}\mathcal{P}_l, \quad l \geqslant 1. \tag{3.9}$$

Here, $0 \leqslant \mathcal{P}_l \leqslant 1$ for all $l \geqslant 1$ and $\alpha_0 = \frac{1}{2}$ such that $\overline{\alpha}(\cos\theta)$ meets the normalization requirement [see Eq. (3.7)] in the isotropic phase where all order parameters vanish.

Inserting Eqs. (3.6) and (3.8) into the expressions for the excess free energy Eqs. (3.3) and (3.4) one can carry out the integrations over orientations of the amphiphilic pair analytically as detailed in Ref. [5]. The final result of these somewhat lengthy and involved derivations can then be cast compactly as

$$\frac{\beta\Delta\mathcal{F}^{\mathrm{ex}}}{V} \equiv \beta\Delta f^{\mathrm{ex}} = \rho^2 \sum_{l=0}^{\infty} \alpha_l^2 u_l \tag{3.10}$$

irrespective of whether we employ the SMF or MMF approximation to the pair correlation function. In Eq. (3.10), Δf^{ex} is the change in free-energy density (relative to that of the hard-sphere reference fluid) caused by the perturbation φ [see Eqs. (2.3)–(2.6)].

As we shall show below in Sec. III B the quantities $\{u_l\}_{l\geqslant 0}$ on the far right side of Eq. (3.10) are related to φ. However, their specific form does depend on whether we invoke the SMF or the MMF approximation to the orientation dependent pair correlation function. In particular, it is possible to derive closed expressions for members of the set $\{u_l\}_{l\geqslant 0}$ if one uses the SMF approximation; within the framework of the MMF approximation the final expressions have to be evaluated numerically.

Next, for the hard-sphere contribution to the free energy in Eq. (3.2) we employ the Carnhan-Starling expression [36]

$$\frac{\beta\mathcal{F}^{\mathrm{hs}}}{V} \equiv \beta f^{\mathrm{hs}} = \rho[\ln(\rho\Lambda^5 m/\mathcal{I}) - 1] + \rho\frac{4\eta - 3\eta^2}{(1-\eta)^2}, \tag{3.11}$$

where $\eta \equiv \rho\sigma^3\pi/6$ is the packing fraction of the hard-sphere reference fluid at density ρ, m is the molecular mass, $\mathcal{I}$ is the moment of inertia of an amphiphile, $\Lambda \equiv \sqrt{\beta h^2/2\pi m}$ is the thermal de Broglie wavelength (h Planck's constant), and the exponent 5 reflects the three translational and two rotational degrees of freedom of the molecular ellipsoids of revolution. Finally, the orientational contribution to $\mathcal{F}$ in Eq. (3.2) is given here by the expression

$$\frac{\beta\Delta\mathcal{F}^{\mathrm{or}}}{V} = \rho\int_{-1}^{1} dx\,\overline{\alpha}(x)\,\ln[2\overline{\alpha}(x)], \tag{3.12}$$

where $x \equiv \cos\theta$. Nonzero values of $\Delta\mathcal{F}^{\mathrm{or}}$ reflect the loss in orientational entropy as a polar phase begins to form. Finally, from Eqs. (3.1), (3.2), (3.10), (3.11), and (3.12) we obtain

$$\begin{aligned}\frac{\beta\Omega}{V} &= \rho[\ln(\rho\Lambda^5 m/\mathcal{I}) - 1] + \rho\frac{4\eta - 3\eta^2}{(1-\eta)^2} \\ &\quad + \rho\int_{-1}^{1} dx\,\overline{\alpha}(x)\,\ln[2\overline{\alpha}(x)] \\ &\quad + \rho^2\sum_{l=0}^{\infty}\alpha_l^2 u_l - \beta\rho\mu,\end{aligned} \tag{3.13}$$

keeping in mind that $\alpha_0 = \frac{1}{2}$ on the last line of Eq. (3.13).

B. Coupling coefficients

To determine the set of coupling coefficients $\{u_l\}_{l\geqslant 0}$ in Eq. (3.10) one expands the functions φ or f in terms of rotational invariants, which has the advantage that one can carry out the integrations over orientations analytically. This approach is described in detail in our earlier publication [5]. Within the SMF approximation one then obtains [see Eq. (3.18) of Ref. [5]]

$$u_l = -\frac{(-1)^l\beta}{\sqrt{\pi}\,(2l+1)^{3/2}}\int_{\sigma}^{\infty} dr_{12}\,r_{12}^2\,\varphi_{ll0}(r_{12}), \quad l \geqslant 0, \tag{3.14}$$

where φ_{ll0} is a coefficient that results from the expansion of φ in terms of rotational invariants and subsequent integration over molecular orientations.

To proceed we restrict ourselves to the quantities u_0 and u_1 throughout this work such that in Eq. (3.14) the expansion coefficients $\varphi_{000}(r_{12})$ and $\varphi_{110}(r_{12})$ are required. To limit ourselves to these two terms is expected to be a reasonably good approximation because they are the leading terms in the expansion Eq. (3.8) [11]. At SMF level and from Eqs. (2.3) and (2.7) it is easy to verify that

$$\varphi_{000}(r_{12}) = \sqrt{4\pi}\varphi_{\mathrm{iso}}(r_{12}), \tag{3.15}$$

where we also used $\Phi_{000} = (4\pi)^{-3/2}$. Employing then Eq. (2.4) together with Eq. (3.15) one finally arrives at

$$u_0 = -\frac{64\pi}{9}\beta\varepsilon\sigma^3. \tag{3.16}$$

In a similar fashion it is easy to show that

$$\varphi_{110}(r_{12}) = 4(4\pi)^{5/2}\sqrt{3}\varepsilon\varepsilon_{\mathrm{H}}\left(\frac{\sigma}{r_{12}}\right)^6, \tag{3.17}$$

which is a direct consequence of the form of φ [see Eqs. (2.3)–(2.6)] and of the orthogonality of the rotational invariants. Inserting this result into Eq. (3.14) and performing the one integration left one obtains

$$u_1 = -\frac{32\pi}{9}\beta\varepsilon\varepsilon_{\mathrm{H}}\sigma^3 \tag{3.18}$$

in agreement with Eq. (3.37) of Ref. [5]. Hence, at SMF level the grand-potential density does not depend on the "dipolar" contribution to φ.

At MMF level [see Eq. (3.4)] we arrive at an expression for u_l similar to Eq. (3.14) where the expansion coefficient φ_{ll0} in the integrand is replaced by the corresponding coefficient f_{ll0}. Notice, that in this case the factor β on the right side of

Eq. (3.14) does not appear on account of Eq. (3.4). To derive expressions corresponding to u_0 and u_1 but at MMF level we proceed as in our earlier work [5] and expand the anisotropic part of the Mayer f function [see Eq. (3.5)] retaining terms up to third order in $\beta\varphi_{\rm anis}$. This yields

$$f_{000}(r_{12}) = (4\pi)^{3/2}\left\{f_{\rm iso}(r_{12}) + [\beta\varphi_{\rm att}(r_{12})]^2 \times \frac{3\varepsilon_{\rm H}^2 + 5\varepsilon_{\rm D}^2}{2}\exp[-\beta\varphi_{\rm iso}(r_{12})]\right\}, \quad (3.19)$$

where

$$f_{\rm iso}(r_{12}) \equiv \exp[-\beta\varphi_{\rm iso}(r_{12})] - 1. \quad (3.20)$$

Inserting this expression into Eq. (3.14) one finally arrives at

$$u_0 = -8\pi\int_\sigma^\infty dr_{12}\, r_{12}^2 f_{\rm iso}(r_{12}) - 4\pi\left(3\varepsilon_{\rm H}^2 + 5\varepsilon_{\rm D}^2\right)\beta^2\mathcal{I}^{(2)}. \quad (3.21)$$

As we already showed in Ref. [5] the corresponding expressions

$$f_{110}(r_{12}) = (4\pi)^{3/2}\sqrt{3}\exp[-\beta\varphi_{\rm iso}(r_{12})] \times\left\{\beta\varphi_{\rm att}(r_{12})\,\varepsilon_{\rm H} + \frac{9}{10}[\beta\varphi_{\rm att}(r_{12})]^3 \times\left(\varepsilon_{\rm H}^3 + 3\varepsilon_{\rm H}\varepsilon_{\rm D}^2 - \frac{1}{3}\sqrt{\frac{10}{3}}\varepsilon_{\rm D}^3\right)\right\} \quad (3.22)$$

and

$$u_1 = \frac{8\pi}{3}\left\{\beta\mathcal{I}^{(1)}\varepsilon_{\rm H} + \frac{9}{10}\beta^3\mathcal{I}^{(3)} \times\left(\varepsilon_{\rm H}^3 + 3\varepsilon_{\rm H}\varepsilon_{\rm D}^2 - \frac{1}{3}\sqrt{\frac{10}{3}}\varepsilon_{\rm D}^3\right)\right\} \quad (3.23)$$

can be obtained in a similar fashion where the integrals

$$\mathcal{I}^{(n)} \equiv \int_\sigma^\infty dr_{12}\, r_{12}^2\,[\varphi_{\rm att}(r_{12})]^n \exp[-\beta\varphi_{\rm iso}(r_{12})] \quad (3.24)$$

in Eqs. (3.21)–(3.23) have to be evaluated numerically. Hence, at MMF level, the resulting expressions for u_0 and u_1 in Eqs. (3.21) and (3.23) depend on both coupling constants $\varepsilon_{\rm H}$ and $\varepsilon_{\rm D}$ unlike their SMF counterparts in Eqs. (3.16) and (3.18).

C. Thermodynamic states

At fixed T thermodynamic equilibrium states of our model are characterized by minima of the grand potential [see Eq. (3.13)] with respect to ρ and $\overline{\alpha}(x)$. Hence, we are seeking simultaneous solutions of the equations

$$\frac{\beta}{V}\left(\frac{\partial\Omega}{\partial\rho}\right) = 0, \quad (3.25a)$$

$$\frac{\beta}{V}\frac{\delta\Omega}{\delta\overline{\alpha}(x)} = \lambda(T,\rho), \quad (3.25b)$$

where λ is a Lagrangian multiplier introduced to ensure that $\overline{\alpha}(x)$ satisfies Eq. (3.7). Using Eq. (3.13) it is straightforward to show that Eq. (3.25a) can be recast as

$$\beta\mu^{\rm hs}(T,\rho) + \int_{-1}^{1} dx\,\overline{\alpha}(x)\ln[2\overline{\alpha}(x)] + 2\rho\sum_{l=0}^{\infty}u_l\alpha_l^2 - \beta\mu = 0, \quad (3.26)$$

where the chemical potential of the hard-sphere fluid is given by

$$\beta\mu^{\rm hs}(T,\rho) \equiv \beta\left(\frac{\partial f^{\rm hs}}{\partial\rho}\right)_{T,V} = \ln(\rho\Lambda^5 m/\mathcal{I}) + \frac{8\eta - 9\eta^2 + 3\eta^3}{(1-\eta)^3}. \quad (3.27)$$

To solve Eq. (3.25b) we invoke the fact that the Legendre polynomials form a complete orthonormal set of functions such that

$$\alpha_l = \frac{2l+1}{2}\int_{-1}^{1} dx\,\overline{\alpha}(x)\,P_l(x). \quad (3.28)$$

Thus, $\overline{\alpha}(x)$ arises in the third and fourth term on the right side of Eq. (3.13). Performing the variational differentiation in Eq. (3.25b) we then have

$$\overline{\alpha}(x) = \frac{1}{2}e^{[\lambda(T,\rho)-\rho]/\rho}\exp\left[-\rho\sum_{l=0}^{\infty}(2l+1)\,u_l\alpha_l P_l(x)\right], \quad (3.29)$$

which automatically satisfies Eq. (3.7) so that

$$\frac{1}{2}e^{[\lambda(T,\rho)-\rho]/\rho} = \frac{1}{\int_{-1}^{1}dx\exp\left[-\rho\sum_{l=0}^{\infty}(2l+1)u_l\alpha_l P_l(x)\right]}. \quad (3.30)$$

With the aid of Eq. (3.29) it is possible to rewrite the third term on the right side of Eq. (3.13) as

$$\int_{-1}^{1} dx\,\overline{\alpha}(x)\ln[2\overline{\alpha}(x)] = \frac{\lambda(T,\rho)-\rho}{\rho} - 2\rho\sum_{l=0}^{\infty}u_l\alpha_l^2, \quad (3.31)$$

where orthogonality of the Legendre polynomials [see Eq. (A.9b) of Ref. [35]] has also been invoked. Inserting this expression into Eq. (3.26) we readily obtain

$$\beta\mu^{\rm hs}(T,\rho) + \frac{\lambda(T,\rho)-\rho}{\rho} - \beta\mu = 0. \quad (3.32)$$

With Eqs. (3.32) and (3.13) can be rewritten more compactly as

$$\frac{\beta\Omega}{V} = \beta f^{\rm hs}(T,\rho) - \rho\beta\mu^{\rm hs}(T,\rho) - \rho^2\sum_{l=0}^{\infty}u_l\alpha_l^2, \quad (3.33)$$

where we also used Eq. (3.31). The last expression is particularly gratifying because it no longer depends on the *a priori* unknown chemical potential μ.

D. Coexisting phases

Suppose now that for a given T two phases $'$ and $''$ exist which are characterized by densities ρ' and ρ'' and orientation distributions $\overline{\alpha}'$ and $\overline{\alpha}''$ and satisfy Eqs. (3.25), that is, they correspond to (local or global) minima of the grand-potential density. At phase coexistence global minima of Ω/V satisfy the conditions

$$\frac{\beta\Omega'}{V} = -\beta P' = -\beta P'' = \frac{\beta\Omega''}{V}, \tag{3.34a}$$

$$\frac{\beta}{V}\frac{\partial\Omega}{\partial\rho}\bigg|_{\rho',\overline{\alpha}'(x)} = \frac{\beta}{V}\frac{\partial\Omega}{\partial\rho}\bigg|_{\rho'',\overline{\alpha}''(x)} = 0, \tag{3.34b}$$

where P' and P'' denote the pressures of the coexisting phases $'$ and $''$, respectively.

Because of Eqs. (3.33) and (3.34a) can be rearranged such that phase coexistence corresponds to zeros of the function

$$\begin{aligned} s_1(T,\rho',\rho'',\{\alpha_l\}) \equiv{}& \beta f^{\mathrm{hs}}(T,\rho') - \beta\rho'\mu^{\mathrm{hs}}(T,\rho') \\ &- \beta f^{\mathrm{hs}}(T,\rho'') + \beta\rho''\mu^{\mathrm{hs}}(T,\rho'') \\ &- \frac{u_0}{4}(\rho'^2 - \rho''^2) + \rho''^2\sum_{l=1}^{\infty} u_l\alpha_l^2, \end{aligned} \tag{3.35}$$

where we tacitly assume phase $'$ always to be isotropic whereas phase $''$ may be isotropic or polar. If phase $''$ is isotropic the sum on the third line of the previous expression vanishes because the entire set of expansion coefficients $\{\alpha_l\}_{l\geqslant 1}$ vanishes identically.

From Eqs. (3.30) and (3.31) we realize that

$$\begin{aligned} &\int_{-1}^{1} dx\,\overline{\alpha}(x)\ln[2\overline{\alpha}(x)] \\ &\quad= -\frac{\rho u_0}{2} - 2\sum_{l=1}^{\infty} u_l\alpha_l^2 + \ln 2 \\ &\qquad - \ln\int_{-1}^{1} dx\,\exp\left[-\rho\sum_{l=0}^{\infty}(2l+1)\,u_l\alpha_l P_l(x)\right] \\ &\quad= -2\sum_{l=1}^{\infty} u_l\alpha_l^2 + \ln 2 - \ln\int_{-1}^{1} dx\,\Psi(x), \end{aligned} \tag{3.36}$$

where we introduced the function

$$\Psi(x) \equiv \exp\left[-\rho\sum_{l=1}^{\infty}(2l+1)\,u_l\alpha_l P_l(x)\right] \tag{3.37}$$

Inserting Eq. (3.36) into Eq. (3.26) we arrive at

$$\beta\mu^{\mathrm{hs}}(T,\rho) + \ln 2 - \ln\int_{-1}^{1} dx\,\Psi(x) + \frac{\rho u_0}{2} - \beta\mu = 0. \tag{3.38}$$

Combining the previous expression with the second of the coexistence conditions Eq. (3.34b) requires us to find the zeros of the function

$$\begin{aligned} s_2(T,\rho',\rho'',\{\alpha_l\}) \equiv{}& \beta\mu^{\mathrm{hs}}(T,\rho') - \beta\mu^{\mathrm{hs}}(T,\rho'') + \frac{u_0}{2}(\rho'-\rho'') \\ &- \ln 2 + \ln\int_{-1}^{1} dx\,\Psi(x). \end{aligned} \tag{3.39}$$

In addition to s_1 and s_2 a unique determination of the unknowns ρ', ρ'', and $\{\alpha_l\}$ requires the solution of l additional equations for the set of order parameters which we obtain as zeros of ($l \geqslant 1$)

$$s_{l+2}(T,\rho',\rho'',\{\alpha_l\}) = \alpha_l - \frac{2l+1}{2}\frac{\int_{-1}^{1} dx\Psi(x)P_l(x)}{\int_{-1}^{1} dx\Psi(x)}. \tag{3.40}$$

Equation (3.40) follows directly from Eqs. (3.28)–(3.30) where we also employed Eq. (3.37). Zeros of the functions $\{s_{l+2}\}_{l\geqslant 1}$ correspond to the order parameters characterizing phase $''$ at phase coexistence. Together the set of $l+2$ equations introduced in Eqs. (3.35), (3.39), and (3.40) can be solved numerically to obtain the complete phase diagram of our amphiphilic model fluid. Details of the numerical procedure can be found in the Appendices.

IV. RESULTS

We now turn to a detailed investigation of the impact of the Heisenberg and "dipolar" coupling parameters ε_{H} and ε_{D} on the phase behavior of our amphiphilic fluid. Phase diagrams will be presented mostly in T-ρ representation where both quantities are expressed in dimensionless (i.e., "reduced") units, that is, T is given in units of $\varepsilon/k_{\mathrm{B}}$, and ρ in units of σ^3. To compare with computer simulations, however, a P-T representation of the phase diagram is advantageous where pressure P is expressed in units of ε/σ^3.

A. Pure Heisenberg fluid

We begin our presentation with the case of the pure classical 3D Heisenberg fluid which is realized in our model by setting $\varepsilon_{\mathrm{D}} = 0$ [see Eqs. (2.3), (2.5), (2.6), and (2.8)]. This part of our study is meant to validate the numerical procedure sketched in the previous section by comparison with earlier work [19,23–32]. We treat the excess free energy at MMF level [see Eq. (3.4)] developed in Sec. III. If the coupling constant $\varepsilon_{\mathrm{H}} = 0.06$ is relatively low the phase diagram presented in Fig. 1(a) shows that a gas coexists with a polar liquid at low T. As T increases the orientational order in the polar phase decreases as one can see from a parallel plot of the polar order parameter $\mathcal{P}_1$ in Fig. 2. Starting at low T the plot in Fig. 2 for $\varepsilon_{\mathrm{H}} = 0.06$ exhibits high values of $\mathcal{P}_1$ which decrease with increasing T. The decline of $\mathcal{P}_1$ with T becomes more and more pronounced until $\mathcal{P}_1$ essentially goes to zero with a nearly infinite slope. At the temperature at which $\mathcal{P}_1$ vanishes a line of critical point starts. Hence, the junction between the isotropic and polar liquid phase boundaries and the critical line is a critical end point. The critical line, which is analogous to

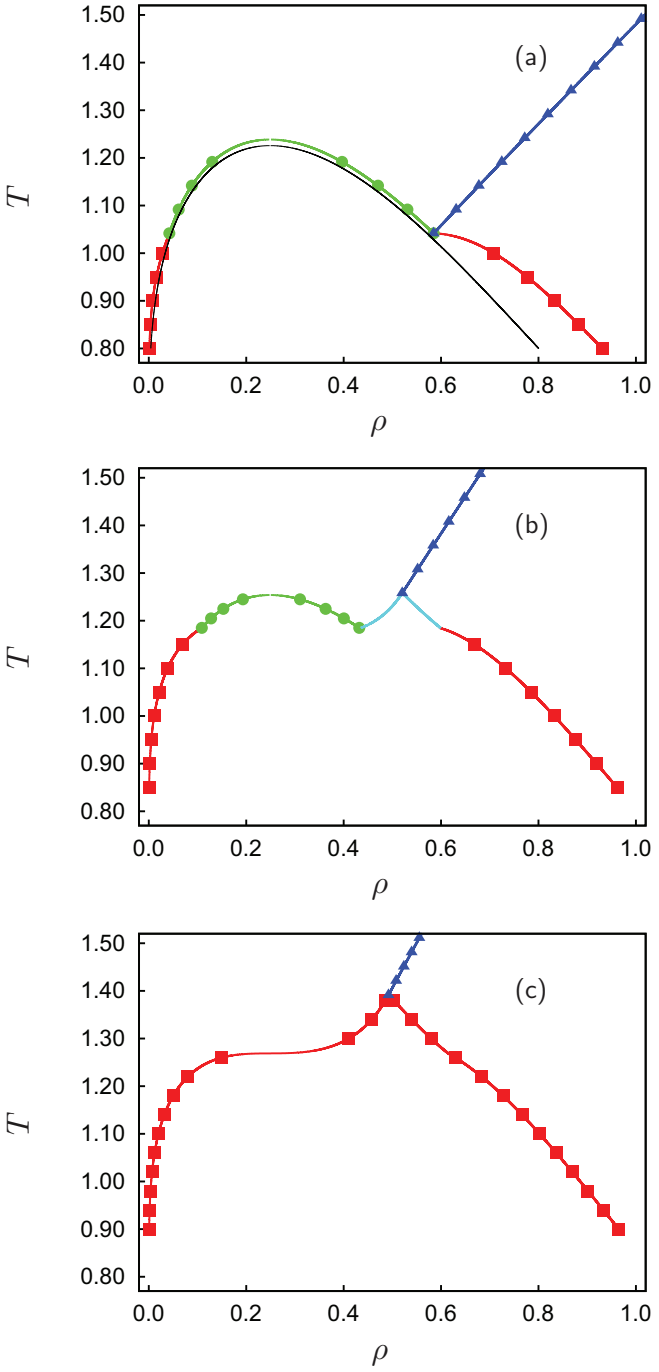

FIG. 1. (Color online) Generic topolgies of phase diagrams for the pure, classical 3D Heisenberg fluid. Solid lines are phase boundaries between gas and polar liquid (■, ——), gas and isotropic liquid (●, ——), and isotropic and polar liquid (——). In addition the line of critical points is shown (▲, ——). (a) Type I at $\varepsilon_H = 0.06$ where we show also data for the special case $\varepsilon_H = 0.00$ (——); (b) type II, $\varepsilon_H = 0.09$; (c) type III, $\varepsilon_H = 0.11$. All curves have been obtained at MMF level (see text).

the Curie line in ferroelectrics, is given by the expression

$$\rho_c = -\frac{2}{3}\frac{1}{u_1} \tag{4.1}$$

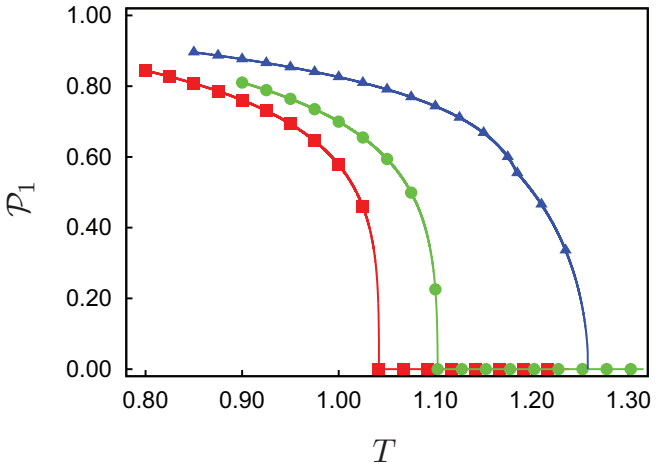

FIG. 2. (Color online) Plot of polar order parameter $\mathcal{P}_1$ as a function of temperature T for $\varepsilon_H = 0.06$ and $\varepsilon_D = 0.00$ (■, ——) [see Fig. 1(a)] and $\varepsilon_D = 0.12$ (●, ——). Also shown are data for $\varepsilon_H = 0.09$ and $\varepsilon_D = 0.00$ (▲, ——) [see Fig. 1(b)]. In all three cases the curves represent state points along the phase boundary of the polar liquid phases.

for the critical density ρ_c as demonstrated earlier by Groh and Dietrich [11], Range and Klapp [16], and more recently by us [5].

For T exceeding that of the critical end point we then find coexistence between a gas and an isotropic liquid in Fig. 1(a). That this liquid phase is isotropic is revealed by the parallel plot of $\mathcal{P}_1$ in Fig. 2, which vanishes and stays at zero until we reach the gas-liquid critical point.

For reasons of comparison we also show in Fig. 1(a) the phase diagram of a fluid with purely isotropic interaction, which is a special case of our amphiphilic fluid realized by $\varepsilon_H = \varepsilon_D = 0$. Hence, interactions beyond the hard-sphere radius are described by the Lennard-Jones potential introduced in Eq. (2.4).

The reason for presenting these data is twofold. First, one notices that the impact of the Heisenberg term on the gas-isotropic liquid envelope of the two-phase region is marginal. Second, the temperature $T_c = 1.2257$ at the gas-liquid critical point for our quasi-Lennard-Jones fluid is only about 6% smaller than that of the true Lennard-Jones fluid where a value of $T_c = 1.3120(7)$ was obtained by Potoff and Panagiotopoulos [37]. On the contrary, the density at the gas-liquid critical point in our model ($\rho_c = 0.250$) is roughly 21% lower than the value $\rho_c = 0.316(1)$ reported by Potoff and Panagiotopoulos for the full Lennard-Jones fluid [37]. Because the critical density is determined by packing effects we suspect that a more satisfactory agreement would be obtainable if a more realistic form of the pair correlation function would have been used in the present study.

For intermediate values of the Heisenberg coupling constant $\varepsilon_H = 0.09$ the plot in Fig. 1(b) reveals a topological change in the phase diagram compared with the situation displayed in Fig. 1(a). Besides coexistence between gas and either an isotropic or a polar liquid phase one also finds coexistence between isotropic and polar liquid phases for intermediate coupling strengths ε_H. This phase coexistence ends at a

tricritical point at which a critical line begins. Along the phase boundary of the polar liquid, $\mathcal{P}_1$ decreases monotonically with increasing T as one can see from the parallel plot in Fig. 2. At the tricritical point $\mathcal{P}_1$ vanishes as expected. At $T = 1.1849$, $d\mathcal{P}_1/dT$ in Fig. 2 exhibits a small discontinuity. The discontinuity corresponds to the junction at which the gas-polar liquid and isotropic-polar liquid branches of the phase diagram meet in Fig. 1(b).

At even larger values $\varepsilon_H = 0.11$ the topology of the phase diagram is different from the two previously discussed ones as one can see by comparing the plot in Fig. 1(c) with plots displayed in Figs. 1(a) and 1(b). Now we have coexistence between a more or less dense gaseous and a polar liquid phase at all temperatures up to the tricritical temperature at which the critical line begins. The gas-liquid critical point is suppressed but its vestige still manifests itself as the rather flat region in the phase diagram centered on $\rho \approx 0.30$.

B. Comparison between simple and modified mean-field theory

After having examined the impact of ε_H on the phase diagram in Sec. IV A it is instructive to compare the prediction of the MMF treatment discussed in that section with the one developed at the much simpler SMF level. We therefore chose the same values of ε_H and plot the SMF phase diagrams in Figs. 3(a)–3(c).

Comparing the plot in Figs. 3(a) with its counterpart shown in Fig. 1(a) shows that at SMF level ε_H is incapable of stabilizing polar liquid phases relative to the isotropic one. A stable polar liquid phase and a line of liquid-liquid critical points arises only at the higher value $\varepsilon_H = 0.09$ as the plot in Fig. 3(b) reveals. At even higher $\varepsilon_H = 0.11$ [see Fig. 3(c)] we obtain a phase diagram at SMF level that is topologically equivalent to the one displayed in Fig. 1(b). Last but not least, at $\varepsilon_H = 0.15$ the topology of the phase diagram at SMF level turns out to be equivalent to the one presented in Fig. 1(c) where the lower coupling constant $\varepsilon_H = 0.11$ was used.

Generally speaking, all three characteristic topologies of phase diagrams are reproduced at SMF level but only for significantly higher values of the Heisenberg coupling constant ε_H. These generic topologies are equivalent to the ones observed earlier in the work of Tavares *et al.* (see their Figs. 1–3) [19].

Another, perhaps more subtle difference between the MMF and the present SMF treatment concerns the location of the gas-liquid critical point. Within the MMF approach one notices a small upward shift of T_c from 1.2257 for $\varepsilon_H = 0.00$ to 1.2539 at $\varepsilon_H = 0.09$. Instead the much simpler SMF approach predicts $T_c \simeq 1.0062$ to be constant over the range $0.00 \leqslant \varepsilon_H \leqslant 0.11$. In addition, at MMF level T_c for $\varepsilon_H = 0.00$ is much closer to the value of T_c for the Lennard-Jones fluid as discussed in Sec. IV A. Moreover, one notices from Eqs. (3.16) and (3.18) that the "dipolar" contribution to φ_{anis} apparently is inconsequential for *any* part of the phase diagram. This is because no term proportional to ε_D survives in the derivation of the SMF expressions for u_0 and u_1 which account for the attractive contribution of the perturbation to the purely repulsive hard-sphere interactions. Hence, we conclude that the more refined treatment of pair correlations introduced by the MMF guarantees a more realistic description of the phase behavior

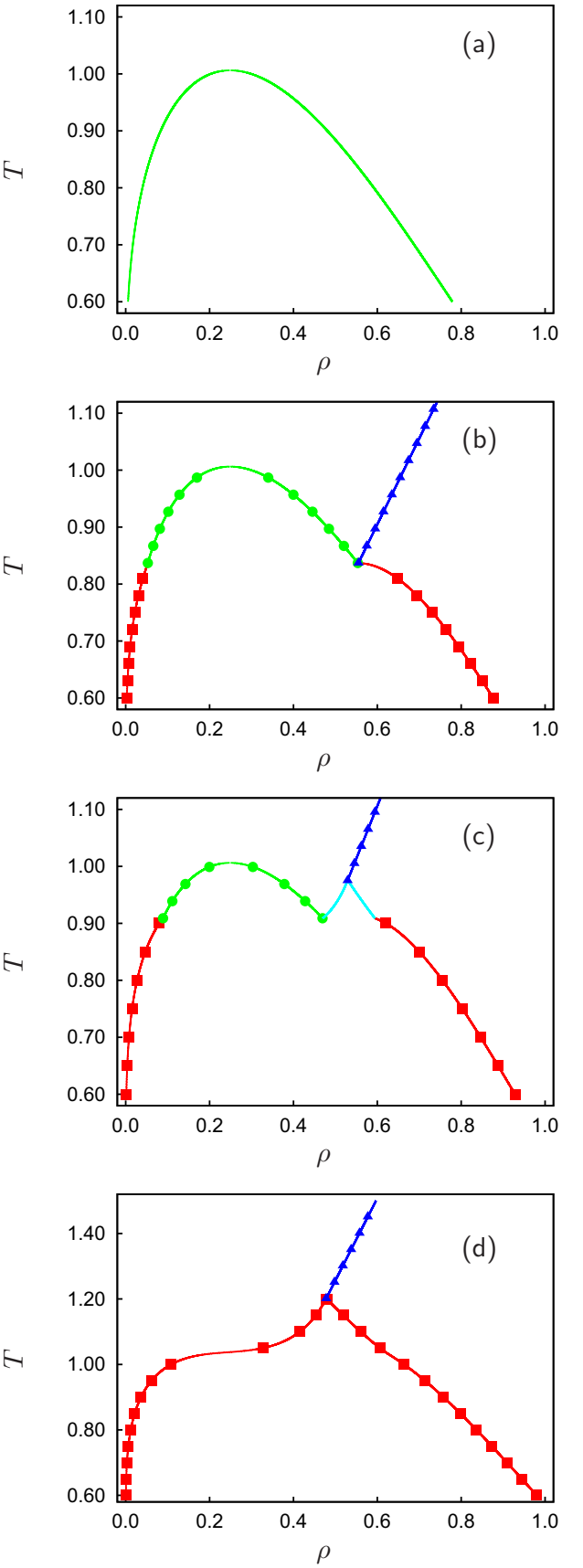

FIG. 3. (Color online) As Fig. 1 but at SMF level. Values of ε_H in parts (a)–(c) are identical with those chosen in Fig. 1(a)–1(c); (d) $\varepsilon_H = 0.15$.

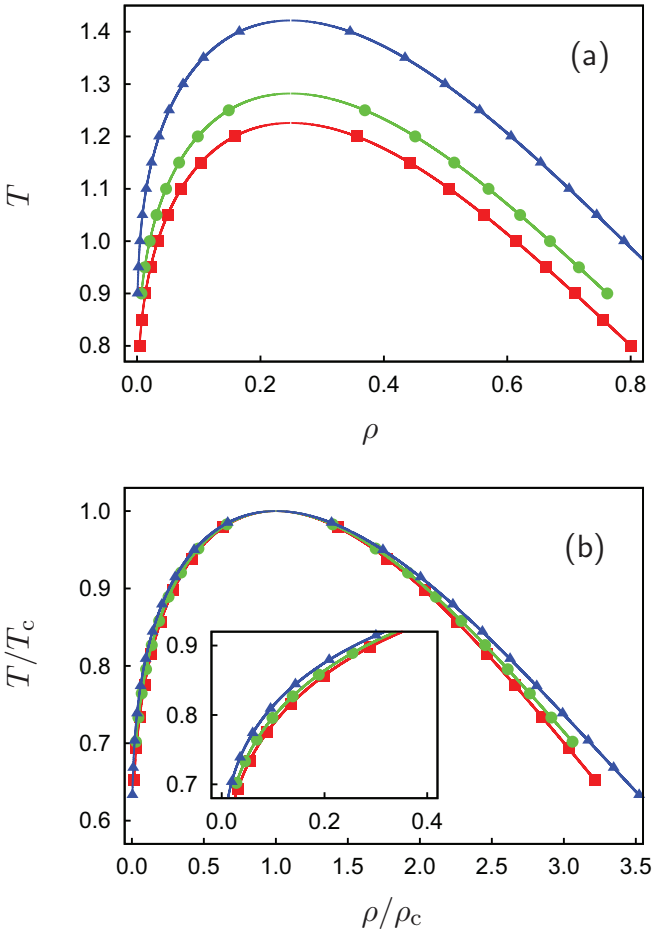

FIG. 4. (Color online) (a) As Fig. 1, but for $\varepsilon_H = 0.00$ and $\varepsilon_D = 0.00$ (■, ——), $\varepsilon_D = 0.10$ (●, ——), and $\varepsilon_D = 0.20$ (▲, ——). (b) As part (a), but in rescaled form where $\rho_c = 0.249$ is the same for all three curves and $T_c = 1.22574$ ($\varepsilon_D = 0.00$), $T_c = 1.28198$ ($\varepsilon_D = 0.10$), and $T_c = 1.42151$ ($\varepsilon_D = 0.20$). In the inset data are plotted on expanded scales to enhance the visibility of the differences between the curves along the phase boundary of the gas.

of our amphiphilic fluid. This is in agreement with earlier assertions for the pure Heisenberg fluid [19] where, however, the interaction potential has a form different from ours. In the subsequent Sec. IV C we will therefore focus on the impact of "dipolar" interactions and analyze which aspect of the phase diagrams is affected by their presence and in what way.

C. The impact of short-range "dipolar" interactions

We begin our discussion of the effect of the "dipolar" contribution to φ_{anis} by presenting in Fig. 4 phase diagrams that are obtained for $\varepsilon_H = 0.00$, that is, by "switching off" the Heisenberg contribution to φ_{anis} [see Eqs. (2.4), (2.5), and (2.6)]. As one realizes from the plots in Fig. 4 a nonzero value of ε_D is not capable of stabilizing polar liquid phases as one of the thermodynamic phases at equilibrium. This was already discussed in our previous work [5] and is attributed to the short-range character of the "dipole-dipole" interactions in our model.

Indeed, in systems composed of "true" dipolar particles, where the interactions decay only as r_{12}^{-3}, a polar phase occurs even in the absence of any short-range van der Waals attraction. The reason is that in an infinite system (i.e., in the absence of boundaries creating a depolarizing field), the long-range dipolar interactions lead to a mean field acting on all particles. This has been seen both in computer simulations (see, e.g., Refs. [8–10]) and DFT calculations [11,16]. At DFT level the presence of the mean field is reflected by the fact that u_1 is nonzero even within the SMF approach [11]. This is clearly in contrast to the present short-ranged model where a dipolar contribution to u_1 occurs only within the MMF treatment if one expands the anisotropic part of the Mayer f function at least up to third order [see Eq. (3.23)].

However, one also sees from Fig. 4(a) that ε_D has a profound effect on the phase diagram in that it shifts the phase boundaries between coexisting gas and isotropic liquid phases upward (i.e., to larger T). This shift reflects that the short-range dipolar interactions, when averaged over orientations, yield an effective isotropic *attraction* between the molecules, an effect which is also reflected by the fact that the MMF expression for u_0 is influenced by ε_D [see Eq. (3.21)]. We also note that a similar, effectively isotropic attraction occurs in systems of true electrostatic or magnetostatic dipoles [11,17,18,38,39]. However, the effect is slightly more subtle as one realizes from the plot of the "reduced" phase diagrams T/T_c versus ρ/ρ_c shown in Fig. 4(b).

In general, it is gratifying to note that sufficiently close to the critical point all three rescaled phase diagrams collapse onto a master curve. This is to be expected because in the vicinity of the critical point details of the intermolecular interactions should not matter. Second, further away from the critical point one realizes that the rescaled phase diagrams cannot be represented by such a master curve. In fact, the two-phase region becomes broader as ε_D increases. This effect is more pronounced along the phase boundary of the isotropic liquid but, as one can see from the inset in Fig. 4(b), is also present along the phase boundary of the amphiphilic gas. Similar deviations from the law of corresponding states have been reported by van Leeuwen for the Stockmayer fluid [39]. Based upon grand canonical ensemble MC simulations it is found there that the gas-liquid coexistence curve cannot be rescaled if the dipole moment varies. However, the effect observed by van Leeuwen seems to extend all the way to the critical point and to exceed the one observed in our model system. Contrary to what was observed by van Leeuwen [39] we find that the law of corresponding states still holds to a reasonably good approximation in the near-critical regime $0.75 \lesssim \rho/\rho_c \lesssim 1.25$.

Based upon the results displayed in both parts of Fig. 4 it seems interesting to investigate the effect of "dipolar" interactions in our model on phase diagrams with a more complex topology. Ideal candidates in this regard are phase diagrams for an intermediate value of ε_H that have been shown in Fig. 1(b) to exhibit phase equilibrium between isotropic and polar liquid phases in excess to the more conventional gas-(isotropic and polar) liquid equilibria.

Generally speaking, an increase of ε_D causes an upward shift of the phase boundaries here as well as one can see from the plot in Fig. 5. This seems very similar to what we observe in the case of topologically simpler phase diagrams (see Fig. 4). However, closer scrutiny reveals that for nonvanishing ε_H the situation is more complex. For example, for $\varepsilon_D = 0.00$

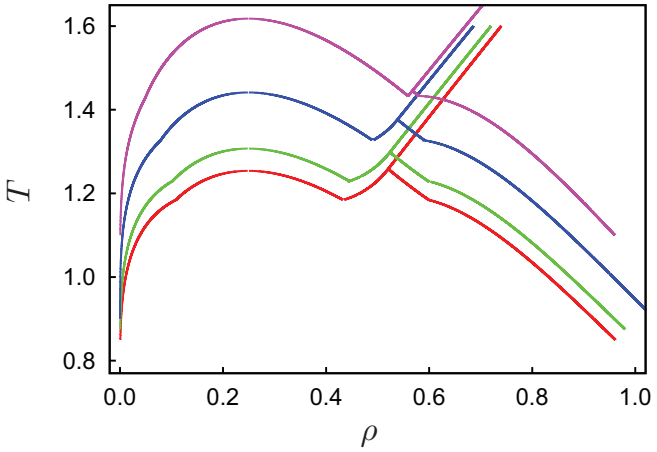

FIG. 5. (Color online) As Fig. 1(b), but from bottom to top for $\varepsilon_D = 0.00$ (—), $\varepsilon_D = 0.10$ (—), $\varepsilon_D = 0.20$ (—), and $\varepsilon_D = 0.30$ (—) (such that $\varepsilon_D = 0.00$ corresponds to the lowest and $\varepsilon = 0.30$ to the top curve, respectively).

the temperature T_{tc} at the tricritical point slightly exceeds the temperature of the gas-isotropic liquid critical point T_c. Moreover, the temperature of the triple point T_{tr} approaches T_{tc} such that *coexisting* isotropic and polar liquid phases eventually disappear.

The variation of these various characteristic temperatures with ε_D is also illustrated by plots in Fig. 6. At small values of ε_D, T_{tc} and T_c are nearly the same. For temperatures lower than these two but higher than T_{tr} one anticipates two discontinuous phase transitions: during the first of these a gas condenses to an isotropic liquid, whereas during the second one the isotropic liquid phase becomes polar. This second transition is accompanied not only by a discontinuous change in the polar order parameter $\mathcal{P}_1$ but also by a similar discontinuity in the density of the liquid. However, this second change in density is relatively small as one can see from Fig. 7. As ε_D increases all three characteristic temperatures increase monotonically. The slope of T_{tc} is smallest such that at sufficiently high ε_D, $T_{tc} \approx T_{tr}$. Thus, ε_D has a destructive impact on liquid-liquid phase

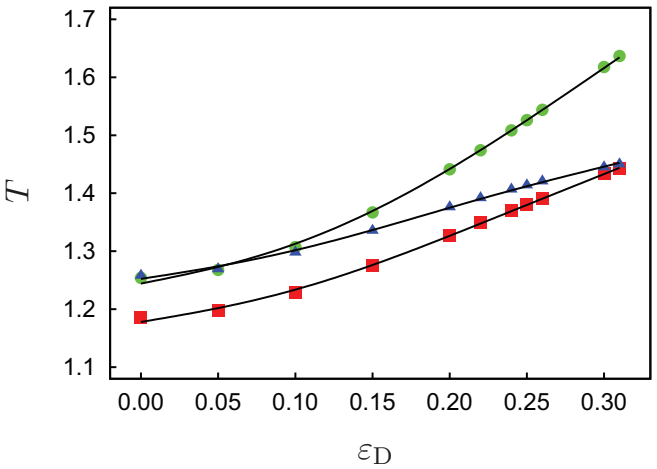

FIG. 6. (Color online) Plots of triple point temperature T_{tr} (■), critical temperature T_c (●), and tricritical temperature T_{tc} (▲) as functions of ε_D and for $\varepsilon_H = 0.09$.

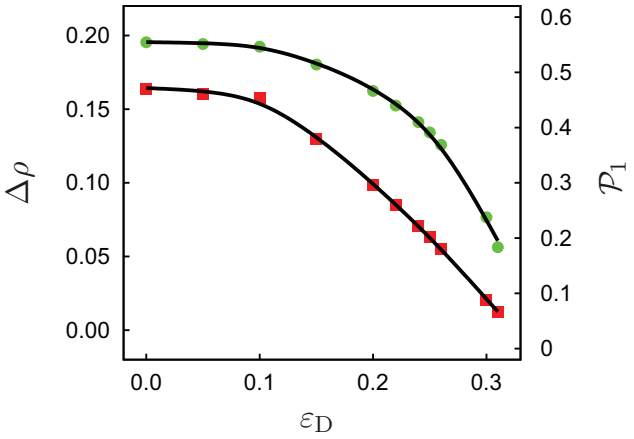

FIG. 7. (Color online) As Fig. 6, but for the density difference $\Delta\rho$ (■) between isotropic and polar liquid phases and the order parameter $\mathcal{P}_1$ (●) in the polar phase ($\varepsilon_H = 0.09$).

equilibrium on the one hand. Among the three characteristic temperatures T_c exhibits the most pronounced increase, which, on the other hand, illustrates a cooperative influence of ε_D on gas-isotropic liquid equilibrium.

The vanishing of the phase boundaries between isotropic and polar liquid phases is also illustrated by plots of the density difference $\Delta\rho$ between coexisting isotropic and polar liquid phases at T_{tr}. With increasing ε_D, $\Delta\rho \to 0$. Simultaneously, $\mathcal{P}_1$ decreases but remains nonzero up to the highest value of $\varepsilon_D = 0.31$ where $\Delta\rho$ has nearly vanished. Thus, plots in Figs. 6 and 7 illustrate a change in the type of phase diagram with increasing ε_D from the prototypical type II [see, for example, Fig. 1(b)] to type I [see, for example, Fig. 1(a)].

V. MONTE CARLO SIMULATIONS

A. Numerical aspects

To gain a deeper insight into the phase behavior of our model fluid and to test the reliability of the MMF approximation we ammend the DFT calculations of this work by Monte Carlo (MC) simulations in which the amphiphiles interact via the potential φ introduced in Eqs. (2.3)–(2.6). The simulations are carried out in the isothermal-isobaric ensemble where a thermodynamic state is uniquely specified by N, P, and T. By employing a conventional Metropolis-type of algorithm the generation of a Markov chain of configurations proceeds in three distinct steps. First, it is decided whether to displace a molecule randomly or to rotate it about a randomly selected axis. Whether or not these processes are accepted is decided on the basis of the associated change in total (configurational) potential energy. We consider each of the N molecules consecutively during this stage of the generation of the Markov chain. Upon its completion one attempt is made to change the volume of the simulation cell. Again an energy criterion is employed to decide upon the acceptance of the volume change. For more details about the algorithm we refer the interested reader to standard textbooks [40,41].

Together the N translation/rotation attempts plus the one attempt to change the system volume constitute a MC cycle. Our results are based upon simulations with an initial 10^4

equilibration cycles followed by 2×10^5 production cycles during which ensemble averages of quantities of interest are computed.

The results presented below are based upon systems containing $N = 1000$ and $N = 5000$ molecules. To save computer time we truncate φ at a cutoff radius of $r_c = 3\sigma$ and employ a combination of Verlet and link-cell lists to maintain a neighbor list set up according to a somewhat larger sphere of radius $r_N = 3.5\sigma$ centered on each molecule. Another molecule is considered to be a neighbor of that reference molecule if the center of mass distance separating each member of the molecular pair is shorter than r_N. The interaction potential remains unshifted at r_c and no corrections are applied for the neglected interactions beyond r_c. To make sure that our results are reliable we compute components of the pressure tensor $\mathbf{P} = P\mathbf{1}$ where the scalar output value of P should agree within a few percent or better with the input value used to generate the Markov chain in the MC simulations. Explicit expressions for diagonal components $P_{\alpha\alpha}$ ($\alpha = x$, y, or z) of $\mathbf{P}$ are given in Eq. (B.6) of Ref. [7]. In addition, we monitor the components $P_{\alpha\alpha}$ individually to make sure that they are equal to within about 3% as they should in the absence of external fields.

Other quantities that we obtain from the MC simulations are the *instantaneous* polar order parameter defined as

$$m \equiv \sum_{i=1}^{N} \hat{\boldsymbol{u}}_i \cdot \hat{\boldsymbol{n}} \tag{5.1}$$

and the second-order cumulant

$$g_2 \equiv \frac{\langle m^2 \rangle}{\langle |m| \rangle^2} \tag{5.2}$$

from the first and second moment of the order-parameter distribution where the angular brackets indicate an average in the isothermal-isobaric ensemble. As explained by Deutsch the magnitude of the instantaneous polar order parameter has to be taken prior to averaging [42]. In Eq. (5.1), $\hat{\boldsymbol{n}}$ is the so-called director which describes the net orientation of the amphiphiles in the polar phase. We compute $\hat{\boldsymbol{n}}$ as the eigenvector associated with the largest eigenvalue of the alignment tensor $\mathbf{Q}$ which we diagonalize numerically by using Jacobi's technique [43] (see also Ref. [44]).

To locate the phase transition between isotropic and polar phases g_2 is a particular useful quantity. If the phase transition is continuous, g_2 for different system sizes have to intersect in a unique, yet model-dependent point which determines the critical point as we explained and demonstrated for the present model in earlier work [7,45]. If, on the other hand, the transition between an isotropic and a polar phase were discontinuous, one would still expect *pairs* of g_2 for different system sizes to intersect in different points depending on what pair of system sizes is considered. In this case the intersections are expected to follow a scaling law such that they become system-size independent if sufficiently large simulation cells are considered [46]. However, if the phase transition is very weakly first-order one may see only a single intersection of *all* cumulants for different system sizes. This is the case for a model related closely to the present one [44].

To make a meaningful comparison between DFT and MC we focus on the most complex type II phase diagram with parameters pertaining to the pure Heisenberg fluid. Specifically, we consider the case represented by $\varepsilon_H = 0.09$ and $\varepsilon_D = 0.00$ for which the DFT results are displayed in Fig. 1(b). To make this comparison we are particularly interested in the pure Heisenberg fluid for a number of reasons. First, it has the topologically richest phase diagram and thus provides the most crucial test case for the DFT calculations. Second, as one can see from Fig. 6 the one-phase region of the isotropic liquid phase is maximized if $\varepsilon_D = 0$. This is because $T_c - T_{tr}$ is largest here. To consider a case with sufficiently large one-phase region of the isotropic liquid is important because this one-phase region is rather small anyway and can easily be missed in the corresponding MC simulations. Third, the pure Heisenberg fluid is interesting because simulation data presented earlier do not predict an isotropic liquid phase and exhibit a Curie line starting at densities lower than the critical density [29,31] whereas in our model the Curie line always starts at densities above the critical densities. We suspect that these finer points depend on details of the interaction potential, which in our case differ from the one used in both earlier works.

B. Comparison between DFT and MC results

Turning now to a comparison between DFT and results obtained in MC we present in Fig. 8 the phase diagram of Fig. 1(b) in P-T representation together with data points obtained in MC simulations. According to the DFT data one expects thermodynamically stable gas, isotropic, and polar liquid phases to occur at $T = 1.22$ whereas the gas is expected to condense directly to a polar liquid phase without an intermittent isotropic liquid phase at the lower $T = 1.05$. For both isotherms we are plotting data that clearly pertain to thermodynamically stable phases. We have been unable to locate with precision the coexistence line separating gas and (isotropic or polar) liquid phases. This is because close to the coexistence line ensemble averages turn out to show

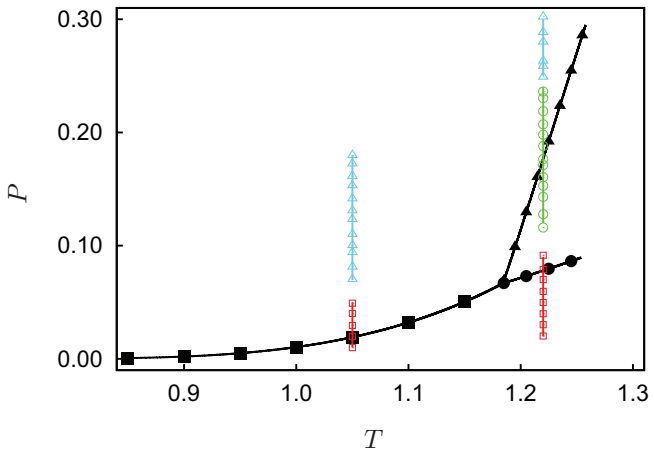

FIG. 8. (Color online) Phase diagram in P-T representation for the case $\varepsilon_H = 0.09$ and $\varepsilon_D = 0.00$ [see also Fig. 1(b)]. Black lines represent coexistence lines from DFT calculations; (■) gas-polar liquid, (●) gas-isotropic liquid, and (▲) isotropic-polar liquid. The critical line is not shown. Open and colored symbols represent results from MC in the respective one-phase region of gas (□), isotropic liquid (○), and polar liquid (△).

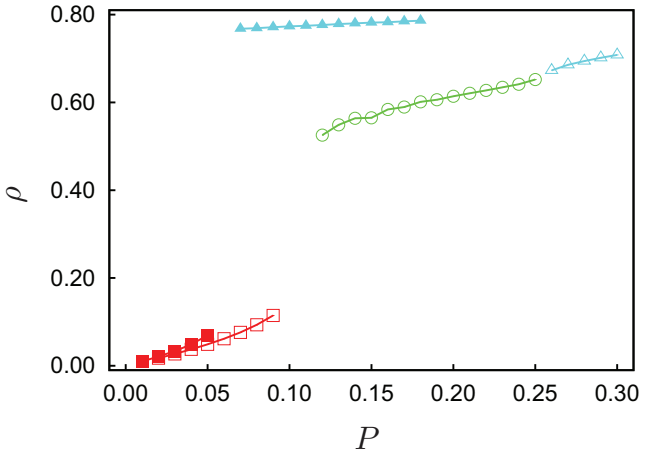

FIG. 9. (Color online) Mean density ρ as a function of pressure P; (■, □) gas, (◯) isotropic liquid, (▲, △) polar liquid. Open symbols refer to $T = 1.22$ whereas filled symbols correspond to $T = 1.05$.

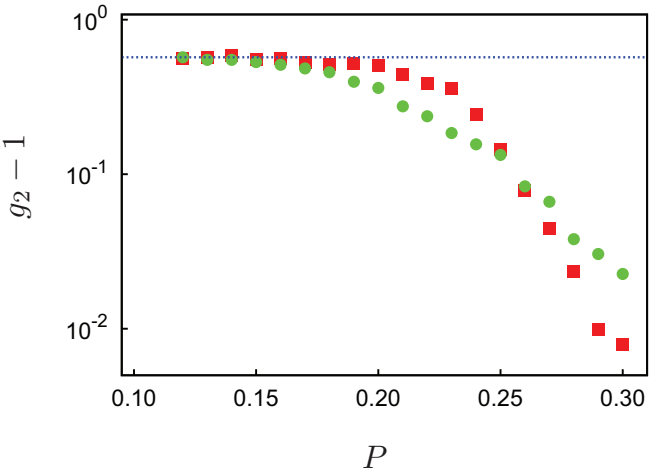

FIG. 10. (Color online) Second order cumulant $g_2 - 1$ as a function of pressure P at $T = 1.22$; (■) $N = 5000$, (●) $N = 1000$, (· · ·) $g_2 - 1 = (\pi - 2)/2$ (see text).

a tiny but noticeable drift even if very long MC runs of 10^6 cycles are employed. Thus, we exclude data points very close to the gas- (isotropic or polar) coexistence. However, generally speaking the topology of the phase diagram obtained by DFT is confirmed by plots in Fig. 8 *qualitatively* on the one hand. *Quantitatively*, on the other hand, it appears that for both temperatures phase transitions obtained in MC occur at somewhat higher pressures compared with the location of DFT coexistence lines.

Moreover, it is instructive to analyze both the mean number density $\rho = N/\langle V \rangle$ (V volume) and the second-order cumulant g_2. Plots of the former in Fig. 9 show the variation of ρ with P for the two isotherms considered. At $T = 1.05$ there is a clear discontinuous change of ρ as the pressure increases. By monitoring $\langle m \rangle$ it is obvious that there is also an associated discontinuous change in the polar order parameter from a low value $\langle m \rangle \simeq 0.007$ at pressures below that at which ρ changes discontinuously to a high value $\langle m \rangle \simeq 0.656$ above that pressure. At $T = 1.22$ there is also a clear discontinuity in the plot of ρ at relatively low P. However, in this case the new phase at higher P is an isotropic liquid.

The latter is inferred from plots in Fig. 10. We restrict the analysis to $N = 1000$ and $N = 5000$ based upon earlier experience with much more detailed finite-size scaling applied to the isotropic-polar phase transition in the present model system [7,45]. These show that even up to $P \lesssim 0.20$ and for $N = 5000$, which is significantly larger than that pressure at which ρ in Fig. 9 exhibits the first discontinuity, $g_2 \simeq \frac{\pi}{2}$, which is the value to be expected in the isotropic phase as explained elsewhere [7,42]. As P increases further both curves shown in Fig. 10 deviate increasingly from this value. The deviation starts at lower P for the smaller system with $N = 1000$. Eventually, both curves intersect at a pressure between $P = 0.25$ and $P = 0.26$ which demarcates the transition to a polar liquid phase as we established earlier [7,45]. From the corresponding plot of ρ in Fig. 9 it seems as if the formation of a polar liquid phase is accompanied by a rather minute discontinuity in the mean density. Hence, we conclude that the formation of the polar phase is very weakly first order. However, comparison between MC data presented in Fig. 9 and the corresponding DFT results shown in Fig. 1(b) reveal that DFT overestimates the change in density at the isotropic to polar liquid phase transition for $T = 1.22$.

VI. DISCUSSION AND CONCLUSIONS

In this work we employ mean-field density functional theory to investigate the phase behavior of an amphiphilic model fluid. We take our molecules to consist of a hard-sphere core of diameter σ and superimpose an anisometric Lennard-Jones perturbation for intermolecular distances $r_{12} \geqslant \sigma$. We consider two separate contributions to the anisotropic attraction. One is identical with the potential describing the interaction between a pair of a classical, three-dimensional Heisenberg "spins," whereas the other one exhibits the orientation dependence of the interaction potential between a pair of (electric or magnetic) point dipoles. Nevertheless, for a fixed relative orientation of a pair of amphiphiles the attraction decays proportional to r_{12}^{-6} and is thus short range.

To treat the contribution of the anisometric Lennard-Jones perturbation to the grand potential we introduce two approximations to the pair correlation function which differ in their degree of sophistication. In the SMF approach pair correlations are completely ignored for all intermolecular distances $r_{12} \geqslant \sigma$. At MMF level we approximate pair correlations in a way that becomes exact in the limit of vanishing fluid density. Whereas at MMF level a subtle interplay of Heisenberg and "dipolar" contributions to the grand potential is obtained the latter do not even come into play at SMF level.

Nevertheless, we observe three types of generic and topologically different phase diagrams within both approximations. These prototypical phase diagrams are observed at different coupling constants ε_{H} depending on whether we work within the SMF or MMF framework. Generally speaking, phase diagrams obtained within the SMF theory exhibit phase boundaries at temperatures significantly lower than those observed if the MMF approximation is invoked. Taking

the hard-sphere reference plus Lennard-Jones perturbation potential as a special case obtained for $\varepsilon_H = \varepsilon_D = 0.00$ we obtain a gas-liquid critical temperature which is only about 6% smaller than that obtained in computer simulations [37]. In the SMF approximation this discrepancy turns out to be about 21%. Hence, we conclude that the MMF approximation is by far superior to the SMF one.

However, it seems noteworthy that the critical density remains the same regardless of the mean-field approximation invoked (SMF versus MMF). This can be ascribed to the fact that at both levels of approximation changes in packing characteristics with changes in the thermodynamic conditions are not accounted for. Hence, to find shifts in critical density as one varies one or both coupling constants ε_H and/or ε_D would require a more refined representation of the pair correlation function. As a first step one could, for example, assume this pair correlation function to be given by that of a hard-sphere fluid at the given density. However, this would be a study in its own right beyond the scope of the present one.

As far as the present work is concerned perhaps the two most important results are the following. As already noted in our previous work [5], the dipolar contribution to the orientation dependent part of the interaction potential alone cannot stabilize polar liquid phases. In fact, this dipolar contribution is almost completely inconsequential for the location of the critical line separating isotropic from polar liquid phases (see Fig. 3 of Ref. [5]). As already mentioned in Sec. IV C this is a consequence of the short-ranged nature proportional to r_{12}^{-6} of the dipolar interactions in our model. However, considering the *whole* phase diagram we realize in this work that the dipolar contribution has an impact on other parts of the phase diagram such as the gas-liquid critical temperature and the width of the two phase region below the critical point.

Second, and even more remarkable is the observation that if polar phases are present on account of a reasonably large coupling constant ε_H, an increase in ε_D may cause the phase boundary separating isotropic from polar liquid phases to vanish altogether. This is because with increasing ε_D the monotonic increase of the tricritical temperature is smaller than that of the triple-point temperature. Hence, at sufficiently large ε_D the two become equal such that the tricritical point becomes a critical end point. Hence, by increasing ε_D we are able to change a phase diagram which was originally of the generic type II into a type I topology, an effect observed here for the first time.

Of course, a strong impact of dipolar interactions on the overall phase behavior is also seen in systems with true, electro- or magnetostatic dipoles whose interaction decays much more slowly (proportional to r_{12}^{-3}). Given these effects it would be interesting to investigate in the future more systematically the role of the range of the interaction potential on the phase behavior of the amphiphilic fluid.

To investigate to what an extent the DFT-generated phase diagrams are realistic we have also carried out MC simulations in the isothermal-isobaric ensemble. This provides a rigorous test because MC may be considered a first-principles method. Because these simulations are rather time consuming we focus on two isotherms in the most complex type II phase diagram where DFT predicts coexistence between gas, isotropic, and polar liquid phases. Our results show that indeed the topology of the DFT phase diagram is confirmed at least qualitatively. However, the deviation between the MC and DFT data shows that the latter is not too far off so that the current MMF DFT can be considered a reliable approach for the present model system. This observation is particularly gratifying because it enables us to apply the DFT developed here not only to the present model system but also to related ones that are capable of describing liquid crystals (see, for example, Ref. [44]).

The modeling of liquid-crystalline materials follows the same general philosophy, namely to take a Lennard-Jones core and to modify the attractive part of the potential according to some properly chosen anisotropy function. Hence, from a simulation point of view this general modeling philosophy is particularly appealing because the molecules remain approximately spherical which guarantees fast equilibration in particular in the grand canonical ensemble where insertion and deletion of particles with substantial shape anisotropy is notoriously difficult.

In the future more detailed computer simulations are planned to gain more insight into the microscopic structure of the participating phases which is not accessible within the present DFT approach. For example, for a related model of Janus particles with a short-range "dipole" the formation of micellar clusters has been reported [47] (see also Ref. [30]). Thus, it would be interesting to see if such clusters would also form within the present model.

ACKNOWLEDGMENTS

We acknowledge financial support from the International Graduate Research Training Group 1524 "Self-assembled Soft Matter Nanostructures at Interfaces." In addition, M.S. is grateful for financial support from the Deutsche Forschungsgemeinschaft through grant Scho 525-9.

APPENDIX A: NUMERICAL SOLUTION OF EQS. (3.35), (3.39), AND (3.40)

To determine the phase diagram Eqs. (3.35), (3.39), and (3.40) need to be solved simultaneously. The $l+2$ equations constitute a system of coupled nonlinear equations where the zeros can be found using the Newton-Raphson iteration scheme (see chapter 9.6 of Ref. [43]).

Suppose we are given a vector $\boldsymbol{x} = (x_1, x_2, \ldots, x_k)$ of variables that have to be determined simultaneously such that they solve the equation

$$\boldsymbol{F}(\boldsymbol{x}) = \boldsymbol{0}, \tag{A1}$$

where $\boldsymbol{F}(\boldsymbol{x})$ is a vector composed of k functions $F_i(\boldsymbol{x})$ $(i = 1, \ldots, k)$ and $\boldsymbol{0}$ denotes the k-dimensional zero vector. In the present case, $\boldsymbol{x} = (\rho', \rho'', \alpha_1, \alpha_2, \ldots)$ and members of $\boldsymbol{F}$ are given by the functions s_1, s_2, …, s_{l+2} specified in Eqs. (3.35), (3.39), and (3.40). Suppose now we are given a vector $\boldsymbol{x} + \delta\boldsymbol{x}$ where $|\delta\boldsymbol{x}| \ll 1$ such that a Taylor expansion of $\boldsymbol{F}$ can be truncated at the linear term, that is,

$$\boldsymbol{F}(\boldsymbol{x} + \delta\boldsymbol{x}) = \boldsymbol{F}(\boldsymbol{x}) + \mathbf{J} \cdot \delta\boldsymbol{x} + O(\delta\boldsymbol{x}^2), \tag{A2}$$

where in the present case the $(l+2)\times(l+2)$ Jacobi matrix of partial derivatives is given by

$$\mathbf{J}(\boldsymbol{x}) = \begin{pmatrix} J_{11} & J_{12} & \dots & J_{1,l+2} \\ J_{21} & J_{22} & \dots & J_{2,l+2} \\ \vdots & & \ddots & \vdots \\ J_{l+2,1} & \dots & \dots & J_{l+2,l+2} \end{pmatrix} \tag{A3}$$

and $J_{ik} \equiv \partial s_i/\partial x_k$.

Setting now $\boldsymbol{F}(\boldsymbol{x}+\delta\boldsymbol{x}) = \mathbf{0}$ in Eq. (A2) we can solve

$$\mathbf{J}(\boldsymbol{x})\cdot\delta\boldsymbol{x} = -\boldsymbol{F}(\boldsymbol{x}) \tag{A4}$$

by LU decomposition using, for example the routines LUDCMP and LUBKSB from Sec. 2.3 of Ref. [43].

Equation (A4) provides the basis for an iterative solution of Eq. (A1) implemented as follows. Suppose, we have an initial vector $\boldsymbol{x}^{(0)}$. Solving Eq. (A4) numerically we obtain a first estimate for $\delta\boldsymbol{x}^{(0)}$ and obtain an improved vector $\boldsymbol{x}^{(1)} = \boldsymbol{x}^{(0)} + \delta\boldsymbol{x}^{(0)}$. Hence, our numerical solution of Eq. (A1) is based upon the successive solution of the pair of equations

$$\begin{aligned} \mathbf{J}(\boldsymbol{x}^{(n)})\cdot\delta\boldsymbol{x}^{(n)} &= -\boldsymbol{F}(\boldsymbol{x}^{(n)}), \\ \boldsymbol{x}^{(n+1)} &= \boldsymbol{x}^{(n)} + \delta\boldsymbol{x}^{(n)}, \quad n = 0,1,\dots. \end{aligned} \tag{A5}$$

In practice, the procedure is halted if $\max\left|\delta\boldsymbol{x}^{(n)}\right| \leqslant 10^{-6}$. If the initial solutions are chosen sensibly, this is achieved in $2-3$ iterations for temperatures smaller by $\Delta T \lesssim 5\times10^{-4}$ than those at the gas-liquid critical point or at the tricritical point of the phase diagram.

We have implemented the iterative solution of Eq. (A1) as follows. As a starting solution we take a sufficiently low initial temperature $T = 0.75-0.9$ and set $\boldsymbol{x}^{(0)} = \left(10^{-4},1.0,1.5\right)$ such that phase $'$ is a dilute gas and phase $''$ is a dense polar liquid initially [for which the initial polar order parameter $\mathcal{P}_1 = 1.0$, see Eq. (3.9)]. With this initial solution we solve Eqs. (A5) until convergence is achieved according to the criterion specified above. We then increase the initial temperature T by a small amount $\Delta T = 10^{-4}$ and take as a new initial solution $\boldsymbol{x}^{(0)}(T+\Delta T) = \boldsymbol{x}^{(n_{\max})}(T)$ where $n_{\max}$ is the maximum iteration number needed for our iterative procedure to converge at temperature T. This procedure is then repeated until the gas-liquid critical or the tricritical point has been reached sufficiently closely.

However, some caution is required for the more complex phase diagram of type II. Initiating the iterative solution as described above the solution of Eqs. (A5) eventually fails at some $T = \widetilde{T}$ at which ρ'' typically exceeds a value of 0.4 and $\alpha_1 > 0$. At $\widetilde{T}$, phase $''$ becomes unstable. One has to reinitiate the iteration procedure according to the following protocol:

(1) Maintain both ρ' and ρ'' at $\widetilde{T}$ but set $\alpha_1 = 0$. With this as a new starting solution one can compute that part of the phase diagram at which gas and isotropic liquid coexist.

(2) Return to $\widetilde{T}$.

(3) Set ρ' to the value ρ'' obtained at $\widetilde{T}$ during the computation of the gas-isotropic liquid branch of the phase diagram.

(4) To determine coexistence between isotropic and polar liquid phases set $\rho'' = 1.0$ and $\alpha_1 = 1.5$ and restart the iteration.

Steps 2–4 allow one to compute that part of the phase diagram along which an isotropic and a polar liquid coexist. If the various branches of the phase diagram connect only insufficiently, they can easily be refined until the desired accuracy is achieved by repeating the above protocol after adjusting the value of $\widetilde{T}$ slightly.

Specializing now to the case $l = 1$, $\mathbf{J}$ reduces to a 3×3 matrix with entries

$$J_{11} = -\frac{1+4(\eta'+\eta'^2-\eta'^3)+\eta'^4}{(1-\eta')^4} - \frac{u_0\rho'}{2}, \tag{A6a}$$

$$J_{12} = \frac{1+4(\eta''+\eta''^2-\eta''^3)+\eta''^4}{(1-\eta'')^4} + \frac{u_0\rho''}{2} + 2\rho''u_1\alpha_1^2, \tag{A6b}$$

$$J_{13} = 2\rho''u_1\alpha_1, \tag{A6c}$$

which one obtains by straightforward differentiation of the expression given in Eq. (3.35). Similarly, we have

$$J_{21} = \frac{\pi}{6}\frac{1+4(\eta'+\eta'^2-\eta'^3)+\eta'^4}{\eta'(1-\eta')^4} + \frac{u_0\rho'}{2}, \tag{A7a}$$

$$J_{22} = -\frac{\pi}{6}\frac{1+4(\eta''+\eta''^2-\eta''^3)+\eta''^4}{\eta''(1-\eta'')^4} - \frac{u_0\rho''}{2} - 2\rho''u_1\alpha_1^2, \tag{A7b}$$

$$J_{23} = -2\rho''u_1\alpha_1, \tag{A7c}$$

and last but not least

$$J_{31} = 0, \tag{A8a}$$

$$J_{32} = \frac{9}{2}u_1\alpha_1\left[1+\frac{\tanh^2(a)-a^2}{a^2\tanh^2(a)}\right], \tag{A8b}$$

$$J_{33} = 1+\frac{9}{2}u_1\rho''\left[1+\frac{\tanh^2(a)-a^2}{a^2\tanh^2(a)}\right], \tag{A8c}$$

where

$$a \equiv 3\rho''\alpha_1u_1. \tag{A9}$$

For the special case of an isotropic phase $''$, $\boldsymbol{x} = (\rho',\rho'',0)$ and therefore the Jacobian matrix given in Eq. (A3) simplifies further to

$$\mathbf{J} = \begin{pmatrix} J_{11} & J_{12} \\ J_{21} & J_{22} \end{pmatrix}, \tag{A10}$$

where the matrix elements are given in Eqs. (A6a), (A6b), (A7a), and (A7b) above.

APPENDIX B: DERIVATION OF EQS. (A8b) AND (A8c)

To derive Eqs. (A8b) and (A8c) for the special case in which we truncate the expansion of the orientation distribution function in Eq. (3.29) after the term corresponding to $l = 1$, we begin by rewriting the general Eq. (3.40) as

$$s_3(T,\rho',\rho'',\alpha_1) = \alpha_1 - \frac{3}{2}\frac{\int_{-1}^{1}dx\,x\,\exp(-3ax)}{\int_{-1}^{1}dx\,\exp(-3ax)} = 0, \tag{B1}$$

where we used the first Legendre polynomial $P_1(x) = x$ and Eqs (3.37) and (A9). It is then easy to verify

that

$$\int_{-1}^{1} dx\ \exp(-3ax) = \frac{2}{a}\sinh(a), \tag{B2a}$$

$$\int_{-1}^{1} dx\ x\ \exp(-3ax) = \frac{2}{a^2}\sinh(a) - \frac{2}{a}\cosh(a), \tag{B2b}$$

from which

$$s_3(T,\rho',\rho'',\alpha_1) = \alpha_1 - \frac{3}{2}\frac{\tanh(a)-a}{a\tanh(a)} = 0 \tag{B3}$$

follows without further ado. Notice in particular that in the special case in which phase $''$ is isotropic, that is for small a [i.e., as $\alpha_1 \to 0$, see Eq. (A9)]

$$\lim_{a\to 0}\frac{\tanh(a)-a}{a\tanh(a)} = \lim_{a\to 0}\frac{\left[a-\frac{1}{3}a^3+O(a^5)\right]-a}{a\left[a-\frac{1}{3}a^3+O(a^5)\right]} \simeq -\frac{1}{3}\lim_{a\to 0} a = 0, \tag{B4}$$

where we have used the expansion of $\tanh(a)$ in a power series for small a [48]. Hence, in the isotropic phase

$$s_3(T,\rho',\rho'',0) = 0 \tag{B5}$$

becomes an identity. Using then Eq. (B3) we notice that

$$J_{32} = -\frac{3}{2}\frac{\partial a}{\partial\rho''}\frac{d}{da}\frac{\tanh(a)-a}{a\tanh(a)} = \frac{9}{2}u_1\alpha_1\left[1+\frac{\tanh^2(a)-a^2}{a^2\tanh^2(a)}\right] \tag{B6}$$

where we also employed Eq. (A9) and the relation $\cosh(a) = 1/\sqrt{1-\tanh^2(a)}$. Similar operations eventually lead to the expression given in Eq. (A8c). In the previous expression

$$\lim_{a\to 0}\frac{\tanh^2(a)-a^2}{a^2\tanh^2(a)} = -\frac{2}{3}, \tag{B7}$$

$$\lim_{a\to\pm\infty}\frac{\tanh^2(a)-a^2}{a^2\tanh^2(a)} = -1 \tag{B8}$$

so that J_{32} and J_{33} are well-behaved quantities everywhere.

[1] A. M. Somoza, E. Chacon, L. Mederos, and P. Tarazona, J. Phys.: Condens. Matter **7**, 5753 (1995).
[2] G. Rosenthal and S. H. L. Klapp, J. Chem. Phys. **134**, 154707 (2011).
[3] G. Rosenthal, K. E. Gubbins, and S. H. L. Klapp, J. Chem. Phys. **136**, 174901 (2012).
[4] J. Hu, S. Zhou, Y. Sun, X. Fang, and L. Wu, Chem. Soc. Rev. **41**, 4356 (2012).
[5] S. Giura, B. G. Márkus, S. H. L. Klapp, and M. Schoen, Phys. Rev. E **87**, 012313 (2013).
[6] T. Erdmann, M. Kröger, and S. Hess, Phys. Rev. E **67**, 041209 (2003).
[7] M. Melle, S. Giura, S. Schlotthauer, and M. Schoen, J. Phys.: Condens. Matter **24**, 209401 (2012).
[8] D. Wei and G. N. Patey, Phys. Rev. Lett. **68**, 2043 (1992).
[9] D. Wei and G. N. Patey, Phys. Rev. A **46**, 7783 (1992).
[10] D. Wei, G. N. Patey, and A. Perera, Phys. Rev. E **47**, 506 (1993).
[11] B. Groh and S. Dietrich, Phys. Rev. E **50**, 3814 (1994).
[12] S. Klapp and F. Forstmann, J. Chem. Phys. **106**, 9742 (1997).
[13] S. H. L. Klapp and G. N. Patey, J. Chem. Phys. **112**, 3832 (2000).
[14] S. Klapp and F. Forstmann, Europhys. Lett. **38**, 663 (1997).
[15] S. H. L. Klapp and G. N. Patey, J. Chem. Phys. **112**, 10949 (2000).
[16] G. M. Range and S. H. L. Klapp, Phys. Rev. E **69**, 041201 (2004).
[17] P. Frodl and S. Dietrich, Phys. Rev. A **45**, 7330 (1992).
[18] P. Frodl and S. Dietrich, Phys. Rev. E **48**, 3203 (1993).
[19] J. M. Tavares, M. M. Telo da Gama, P. I. C. Teixeira, J. J. Weis, and M. J. P. Nijmeijer, Phys. Rev. E **52**, 1915 (1995).
[20] C. Spöler and S. H. L. Klapp, J. Chem. Phys. **118**, 3628 (2003).
[21] M. Gramzow and S. H. L. Klapp, Phys. Rev. E **75**, 011605 (2007).
[22] S. H. L. Klapp and M. Schoen, J. Chem. Phys. **117**, 8050 (2002).
[23] J. S. Høye and G. Stell, Phys. Rev. Lett. **36**, 1569 (1977).
[24] P. C. Hemmer and D. Imbro, Phys. Rev. A **16**, 380 (1977).
[25] L. Feijoo, C.-W. Woo, and V. T. Rajan, Phys. Rev. B **22**, 2404 (1980).
[26] R. M. Stratt, Phys. Rev. Lett. **53**, 1305 (1984).
[27] P. de Smedt, P. Nielaba, J. L. Lebowitz, J. Talbot, and L. Dooms, Phys. Rev. A **38**, 1381 (1988).
[28] D. Marx, P. Nielaba, and K. Binder, Phys. Rev. Lett. **67**, 3124 (1991).
[29] E. Lomba, J. J. Weis, and G. Stell, Phys Rev. E **50**, 3853 (1994).
[30] E. Lomba, J. L. López-Martin, H. M. Cataldo, and C. F. Tejero, Phys. Rev. E **49**, 5164 (1994).
[31] J. J. Weis, M. J. P. Nijmeijer, J. M. Tavares, and M. M. Telo da Gama, Phys. Rev. E **55**, 436 (1997).
[32] T. G. Sokolovska, Physica A **253**, 459 (1998).
[33] T. G. Sokolovska and R. O. Sokolovskii, Phys. Rev. E **59**, R3819 (1999).
[34] A. J. Stone, Mol. Phys. **36**, 241 (1978).
[35] C. G. Gray and K. E. Gubbins, *Theory of Molecular Fluids*, Vol. 1 (Clarendon Press, Oxford, 1984).
[36] N. F. Carnahan and K. E. Starling, J. Chem. Phys. **51**, 635 (1969).
[37] J. J. Potoff and A. Z. Panagiotopoulos, J. Chem. Phys. **109**, 10914 (1998).
[38] P. I. Teixeira and M. M. Telo da Gama, J. Phys.: Condens. Matter **3**, 111 (1991).
[39] M. E. van Leeuwen, Mol. Phys. **82**, 383 (1994).
[40] M. P. Allen and D. J. Tildesley, *Computer Simulations of Liquids* (Clarendon Press, Oxford, 1987), Chap. 4.5.
[41] D. Frenkel and B. Smit, *Understanding Molecular Simulations* (Academic Press, London, 2002), Chap. 5.4.
[42] H. P. Deutsch, J. Stat. Phys. **67**, 1039 (1992).

[43] W. T. Press, S. A. Teukolsky, W. T. Vetterling, and B. P. Flannery, *Numerical Recipes in FORTRAN 90* (Cambridge University Press, Cambridge, 1996).
[44] M. Greschek and M. Schoen, Phys. Rev. E **83**, 011704 (2011).
[45] M. Melle, S. Giura, S. Schlotthauer, and M. Schoen, J. Phys.: Condens. Matter **24**, 035103 (2012).
[46] H. Weber, W. Paul, and K. Binder, Phys. Rev. E **59**, 2168 (1999).
[47] F. Sciortino, A. Giacometti, and G. Pastore, Phys. Rev. Lett. **103**, 237801 (2009).
[48] I. N. Bronstein, K. A. Semendjajew, G. Musiol, and H. Mühlig, in *Taschenbuch der Mathematik*, 5th ed. (Harri Deutsch, Thun und Frankfurt am Main, 2001), p. 1045.